Tensorial elastodynamics for coupled acoustic/elastic anisotropic media: incorporating bathymetry

Harpeet Sethi, Jeffrey Shragge [ID] and Ilya Tsvankin

Center for Wave Phenomena, Department of Geophysics, Colorado School of Mines, Golden, CO 80401, USA. E-mail: hsethi@mines.edu

SUMMARY

Correctly implementing the fluid/solid boundary conditions at the seafloor is important for accurate full-wavefield imaging and inversion of marine seismic data. Because bathymetric profiles are rarely flat, the associated undulations influence wave modes interacting with the seafloor and, therefore, the ensuing imaging and inversion results. The conventional method of using single-domain elastic finite-difference (FD) solutions assumes that the fluid/solid contact is welded, which leads to incorrect handling of the boundary conditions and introduces modelling errors. We present a mimetic finite-difference (MFD) approach to solve the equations of anisotropic elastodynamics in a non-orthogonal coordinate system conformal to the bathymetric interface. The vertically deformed coordinate mapping transforms the irregular Cartesian (physical) domain into a regularly sampled generalized computational domain. We partition the medium into the acoustic and elastic subdomains and explicitly satisfy the fluid/solid boundary conditions with a split-node approach involving high-order one-sided MFD operators that achieve uniform spatial accuracy throughout the computational domain. Fully staggered grids (FSGs) are used to solve the velocity–pressure and velocity–stress formulations of the acoustic and anisotropic elastic wave equations, respectively. Numerical examples demonstrate that the proposed MFD+FSG algorithm accurately simulates wavefields even for strongly undulating bathymetric surfaces overlying structurally complex anisotropic media, and produces no spurious numerical artefacts (e.g. staircasing) or unphysical wave modes often caused by improper handling of the strong-contrast bathymetric interface. The wavefields generated by the tensorial MFD scheme closely match those from the more computationally expensive spectral-element method used to validate our implementation. The developed MFD+FSG technique can be effectively employed as the modelling kernel in a variety of coupled acoustic/elastic imaging and inversion applications.

Key words: Elasticity and anelasticity; Numerical modelling; Acoustic properties; Interface waves; Seismic anisotropy; Wave propagation.

1 INTRODUCTION

Modelling seismic wavefields that propagate across irregular interfaces is of significant practical interest in processing of both marine and land seismic surveys. Handling curved boundaries using regular Cartesian grids remains challenging and gives rise to such numerical artefacts as staircase diffractions. For marine seismic, an additional challenge is accurately handling the fluid/solid boundary in the presence of seafloor bathymetry. The conventional approach—treating the fluid medium as a solid with zero shear wave velocity—leads to the incorrect boundary conditions at this interface and inaccurate energy partitioning for body waves, as well as to phase and amplitude distortions for Scholte (de Hoop & Van der Hijden 1984; Singh *et al.* 2021) and leaky Rayleigh (Padilla *et al.* 1999) modes.

A number of numerical and semi-analytic methods have been developed to compute elastic wavefields in the presence of an irregular fluid/solid interface. Semi-analytic approaches, such as the generalized reflection/transmission coefficient method (Ge & Chen 2007), can be used only for a stack of homogeneous layers separated by irregular interfaces, and the extension to heterogeneous models is challenging to implement. Van Vossen *et al.* (2002) discuss a finite-difference (FD) modelling approach that uses a single global elastic wave propagator for a medium composed of fluid and solid layers. They observe errors in the simulated seismograms when the fluid/solid interface is not aligned with the grid; Scholte waves are incorrectly modelled even when the grid and the interface are aligned.

Apart from the noted physical inaccuracy, the computational cost of an anisotropic elastic finite-difference (FD) solver, as defined by the number of the partial wavefield derivatives to be computed, is approximately five (for 2-D) and eight (for 3-D) times greater than that of

an acoustic FD propagator of the same approximation order at the equivalent discretization interval. (We point out that models with high *P*-to *S*-wave velocity ratios require a finer discretization of the solid domain compared to the fluid domain. Therefore, the computational cost of elastic modelling would be significantly higher than that of acoustic modelling due to the discretization interval requirements.) Thus, when computing FD-based elastic wavefields in marine settings, it is desirable to use an acoustic wave propagator for the water layer, an elastic propagator for the underlying medium, and satisfy the boundary conditions at the fluid/solid bathymetric interface.

One strategy to achieve this is to use a partitioned-grid approach where the acoustic wave equation in the fluid and the elastic wave equation in the solid are solved on separate grids that are coupled at the domain boundary (Komatitsch *et al.* 2000; Käser & Dumbser 2008; Sun *et al.* 2017; Singh *et al.* 2021). Zhang (2004) employs the finite-element method on a partitioned grid for wavefield modelling in the presence of a fluid/solid interface and uses an integral approach to implicitly satisfy the boundary conditions. To compute elastic wavefields for irregular fluid/solid interfaces, Käser & Dumbser (2008) and Wilcox *et al.* (2010) use the discontinuous Galerkin method, whereas Voinovich *et al.* (2003) employ the finite-volume method. Komatitsch *et al.* (2000) and Chaljub *et al.* (2003) develop spectral-element methods (SEMs) to model wave propagation in fluid/solid configurations and achieve the spatial accuracy greater than $O(\Delta x^4)$ [where $O(\Delta x^n)$ denotes the *n*th-order spatial accuracy]. However, their scheme is computationally expensive and uses a complicated meshing procedure for creating boundary-conforming grids. Overall, the algebraic complexity and computational and memory costs of these high-end techniques prevent their routine application in solving large-scale 3-D anisotropic elastic wavefield modelling and inversion problems.

FD methods are commonly employed along with staggered grids (and their variants) for modelling elastic wavefields. Standard staggered grids (SSGs) are now routinely applied to elastic modelling in isotropic media (Virieux 1986). However, the extension of the SSG+FD methods to arbitrarily anisotropic media involves interpolating partial derivative wavefields, which results in increased computational time, loss of accuracy, and could cause numerical instabilities. Fully staggered grids (FSGs, also known as Lebedev grids) are often used with FD schemes for anisotropic media because multiple subgrids eliminate interpolation issues and help to achieve higher accuracy and improved stability compared to SSG approaches. However, employing multiple subgrids means that FSG techniques are roughly two (2-D) or four (3-D) times more computationally expensive and have greater memory complexity than SSG schemes (Lisitsa & Vishnevskiy 2010). In general, the benefits for most of the FD-based techniques include a straightforward implementation, compact stencils for computing higher order derivatives that port well to GPU architectures, and a moderate computational cost, the combination of which makes them an attractive option for industry-scale applications.

The extension of FD methods to curvilinear grids (Fornberg 1988; Tessmer *et al.* 1992; Hestholm & Ruud 1994; Zhang & Chen 2006; Appelö & Petersson 2009; Tarrass *et al.* 2011; de la Puente *et al.* 2014; Shragge 2017) makes it possible to handle irregular interfaces and avoid unphysical artefacts (e.g. staircase diffractions). In addition, mimetic FD operators can be used to implement the boundary conditions using specially designed stencils and achieve uniform accuracy throughout the entire computational domain (Castillo & Miranda 2013; de la Puente *et al.* 2014; Shragge & Konuk 2020; Singh *et al.* 2021).

Modelling wave propagation with FD operators across curved bathymetric surfaces can be implemented by solving the governing wave equations directly on the deformed grids conformal to interfaces using a chain-rule approach that transforms the partial wavefield derivatives from curvilinear to Cartesian coordinates (Hestholm & Ruud 1994; de la Puente *et al.* 2014; Sun *et al.* 2017). However, this methodology is computationally expensive because it requires additional partial-derivative calculations (Komatitsch *et al.* 1996).

Alternatively, wave equations can be solved directly on curved grids using a tensorial formulation that is independent of a coordinate system. Depending on the coordinate mapping or computational method applied, this approach can involve computing the same number of partial wavefield derivatives as for Cartesian coordinate solutions. However, additional memory is needed to store the geometry-related fields (Komatitsch *et al.* 1996), unless one follows the semi-analytic formulation of Shragge & Konuk (2020) for vertically deformed meshes. The tensorial approach has been developed for elastic isotropic (Komatitsch *et al.* 1996; Shragge & Konuk 2020) and anisotropic models (Konuk & Shragge 2021) with free-surface topography; however, we are unaware of any applications involving coupled media in the presence of irregular bathymetry.

In this paper, we present a novel contravariant formulation of tensorial elastodynamics that extends the approach of Shragge & Konuk (2020) to coupled acoustic/elastic anisotropic models with bathymetry. We partition the medium into the fluid and solid subdomains and solve the respective acoustic and elastic wave equations using mimetic finite-difference (MFD) operators on FSGs. The two subdomains are coupled at the internal bathymetric interface by satisfying the fluid/solid boundary conditions with a split-node approach (Singh *et al.* 2021).

The paper begins with a review of the tensorial theory of acousto- and elastodynamics and the boundary conditions for a fluid/solid interface. Then, we present an analytic description of the generalized family of vertically deformed coordinate systems and specify a particular coordinate transformation based on quadratic Bézier interpolants that automatically maps bathymetry to a surface-conforming grid. Next we discuss the numerical implementation of the proposed technique including the application of the MFD+FSG approach to incorporate the fluid/solid boundary conditions. Numerical examples for 2-D models with curvilinear fluid/solid interfaces illustrate the accuracy of our tensorial MFD method for both isotropic and anisotropic elastic media.

2 THEORY

The coupled acoustic/elastic MFD+FSG approach for complex bathymetry involves tensorial representations of acousto- and elastodynamics and implementation of the fluid/solid boundary conditions at the bathymetric interface. The tensorial approach operates in a generalized

but uniformly sampled 2-D coordinate system $\boldsymbol{\xi}$ that represents the model in the computational domain, which is related to an underlying Cartesian mesh $\mathbf{x}$ that represents the model in the physical space. The two domains are connected via smooth and invertible forward and inverse transformations, $\xi^i = \xi^i(\mathbf{x})$ and $x^i = x^i(\boldsymbol{\xi})$. The superscript or raised indices represent contravariant representation and subscript or lowered indices represent covariant representation of the tensors. The reader is referred to Appendix A for a review of the tensorial calculus used in the development of our MFD approach. Shragge & Tapley (2017) and Shragge & Konuk (2020) ,respectively, present more complete developments of tensorial acousto- and elastodynamics.

2.1 Tensorial elastodynamics

The tensorial formulation of elastodynamics involves specifying three governing equations: (1) conservation of linear momentum; (2) a stress–strain constitutive relationship and (3) an infinitesimal strain-displacement approximation. Conservation of linear momentum in a heterogeneous anisotropic elastic medium can be described in the following contravariant form (Brillouin & Brennan 1965; Flügge 1972; McConnell 2014):

$$\rho_s \dot{v}^i = \nabla_j \sigma^{ij} + f^i, \tag{1}$$

where ρ_s is the density, v^i is the ith contravariant component of the particle-velocity vector, a dot above a variable denotes the temporal derivative, σ^{ij} is the second-order contravariant stress tensor and f^i is the contravariant body force per unit volume. Throughout the manuscript, we assume the summation convention where indices range over $i, j = 1, 2$ for the 2-D implementation. The covariant derivative ∇_j of the contravariant stress tensor σ^{ij} in eq. (1) can be expanded as:

$$\nabla_j \sigma^{ij} = \sigma^{ij}_{,j} + \Gamma^i_{jl}\sigma^{lj} + \Gamma^j_{jl}\sigma^{il}, \tag{2}$$

where $\sigma^{ij}_{,j}$ represents the partial derivative of σ^{ij} with respect to ξ^j, and Γ^i_{jl} are the Christoffel symbols of the second kind, which are defined in eq. (A4) using the metric tensor g_{ij} in eq. (A1).

The second equation is the linear constitutive relationship (i.e. Hooke's law) that links the contravariant stress- and covariant strain-rate tensors, $\dot{\sigma}^{ij}$ and $\dot{\epsilon}_{kl}$, through

$$\dot{\sigma}^{ij} = C^{ijkl} \dot{\epsilon}_{kl}, \tag{3}$$

where C^{ijkl} is the fourth-order contravariant stiffness tensor.

Finally, assuming infinitesimal displacements (i.e. $\nabla_l v_k \ll 1$), the third governing equation can be written as:

$$\dot{\epsilon}_{kl} = \frac{1}{2}\left(\nabla_l v_k + \nabla_k v_l\right) = \frac{1}{2}\left(v^k_{,l} + v^l_{,k}\right) - \Gamma^i_{kl}v_i, \tag{4}$$

where v_k and v_l are the covariant components of the particle-velocity vector; here, we have exploited the symmetry properties of the Christoffel symbols (i.e. $\Gamma^i_{kl} = \Gamma^i_{lk}$).

In this contravariant representation of elastodynamics, all fields retain the well-known tensorial symmetry properties (i.e. $\sigma^{ij} = \sigma^{ji}$, $\epsilon_{kl} = \epsilon_{lk}$, $C^{ijkl} = C^{jikl} = C^{ijlk} = C^{ijlk} = C^{klij}$), which yields the expected maximum of 21 independent stiffness coefficients for the most general (triclinic) anisotropy. Finally, the relationship between the covariant particle-velocity components in eq. (4) and the contravariant components in eq. (1) can be established using the rank-one tensor index-raising operation (see eq. A6).

2.2 Tensorial acoustodynamics

The equations of motion in an inviscid fluid are governed by the conservation of linear momentum and mass. For a generalized coordinate system, these equations can be written as:

$$\rho_f \dot{v}^i_f + g^{ij}\frac{\partial p}{\partial \xi^j} = 0 \tag{5}$$

and

$$\dot{p} + \rho_f c_f^2 \nabla_i v^i_f = 0, \tag{6}$$

where p is the pressure, ρ_f is the fluid density, c_f is the fluid velocity, v^i_f is the contravariant component of the particle velocity, and g^{ij} is the contravariant metric tensor defined in eq. (A2). The covariant derivative of the contravariant vector is defined in eq. (A15).

2.3 Fluid/solid boundary conditions

The boundary conditions coupling acoustic and elastic media are the continuity of traction and of the normal component of the particle velocity, respectively known as the dynamic and kinematic boundary conditions. The continuity of traction is given by:

$$\sigma^{ij}n_j = -pI^{ij}n_j, \tag{7}$$

where I^{ij} is the unit contravariant tensor, p is pressure and n_j is the unit vector normal to the bathymetric surface. The continuity of the normal component of the particle velocity is expressed as:

$$v_i^f n_i = v_i^s n_i. \tag{8}$$

Note that eqs (7) and (8) form a system of equations for an irregular fluid/solid interface because, in contrast to the flat seafloor case, the normal n_j is not necessarily vertically oriented.

The boundary condition at the top of the acoustic layer (i.e. at the water–air interface) requires setting

$$p = 0 \tag{9}$$

for all nodes located on the free surface.

3 VERTICALLY DEFORMED COORDINATE SYSTEMS

One of the challenges in generating FD solutions on curvilinear grids is choosing an optimal coordinate mapping. While there are numerous approaches to creating meshes, herein we use a family of non-orthogonal coordinate transformations that allows computational grids to be specified *implicitly* using minimal information about the controlling surfaces. This approach significantly reduces memory requirements because one does not need to hold any coordinate system or geometric field in memory, except for the bathymetric profile itself. The resulting meshes are deformed only in the vertical (depth) direction ξ^1, but effectively remain Cartesian in the lateral direction ξ^2.

The family of 2-D vertically deformed coordinate systems (Shragge & Tapley 2017; Shragge & Konuk 2020) is defined by:

$$\mathbf{x} = \begin{bmatrix} x^1 \\ x^2 \end{bmatrix} = \begin{bmatrix} F(\xi^1, \xi^2) \\ \xi^2 \end{bmatrix}, \tag{10}$$

where $F(\xi^1, \xi^2)$ is a generalized function representing vertical deformation, an example of which is presented below.

As discussed above, the tensorial wave equation includes the inverse metric tensor g^{ij}, the determinant of the covariant metric tensor $|g_{ij}|$, and the Christoffel symbols of the second kind Γ^i_{jl}. For the transformation in eq. (10), the inverse metric (contravariant) tensor is:

$$g^{ij} = \frac{1}{F_1} \begin{bmatrix} F_1^{-1}(1 + F_2^2) & -F_2 \\ -F_2 & 1 \end{bmatrix}, \tag{11}$$

where F_i represents the partial derivative of F with respect to ξ^i. The square root of the metric (covariant) tensor determinant is:

$$\sqrt{|g_{ij}|} = F_1. \tag{12}$$

The associated Christoffel symbols of the second kind are:

$$\begin{bmatrix} \Gamma^1_{jk} \\ \Gamma^2_{jk} \end{bmatrix} = \frac{1}{F_1} \begin{bmatrix} F_{j,k} \\ 0 \end{bmatrix}, \tag{13}$$

where $F_{j,k}$ represents a second-order partial derivative.

3.1 Vertically deformed tensorial elastodynamics

In eqs (2) and (4), the Christoffel symbols are associated with the field variables σ_{ij} and v_i. However, in staggered grid implementations, the partial derivatives of the field variables are defined at grid points that are staggered from the grid where the field variables are specified. Using eq. (13) for Christoffel symbols, we can rewrite, for example, eq. (4) in the form:

$$\Gamma^1_{kl} v_i = \frac{1}{F_1} \left[F_{k,l} \right] v_i. \tag{14}$$

A chain-rule approach allows us to shift the partial derivatives from the coordinate to the particle-velocity field:

$$F_{k,l} v_i = (F_k v_i)_{,l} - F_k v_{i,l}. \tag{15}$$

Now eq. (14) can be written as:

$$\Gamma^1_{kl} v_i = \frac{1}{F_1} \left[(F_k v_i)_{,l} - F_k v_{i,l} \right]. \tag{16}$$

Note that eq. (16) contains only the partial derivatives of particle velocity. The chain-rule transformation allows us to replace the field variables associated with the Christoffel symbols with the partial wavefield derivatives, and all terms in eqs (2) and (4) are now defined on the same staggered grids.
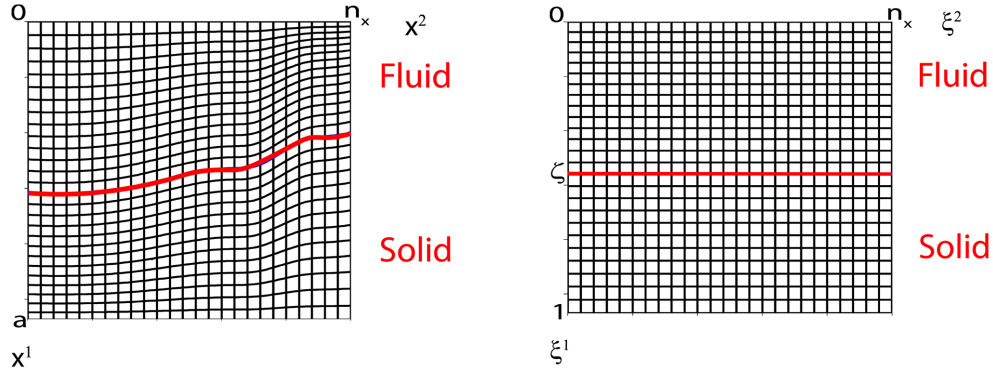
Figure 1. Illustration of the coordinate mapping. (a) The physical Cartesian coordinate system. (b) The generalized regularly sampled computational mesh. The thicker red lines mark the bathymetric surface defined at the coordinate level $\xi^1 = \zeta$ and mapped to flat layers in the computational mesh.

3.2 Bathymetric coordinate system

We generate an analytic coordinate system based on quadratic Bézier interpolation that uses three control interfaces (see Appendix B for details). The bathymetric surface is regularly sampled in the lateral direction and described in a parametric form for 2-D problems as $B(\xi^2)$. The employed mapping defines the undulating bathymetry in the physical domain **x**. The irregular physical mesh is mapped to a regular computational mesh (where bathymetry conforms to a single flat pseudo-depth surface) in the generalized coordinate system ξ. To generate a C^2-diffeomorphic (i.e. smooth, differentiable and invertible) mesh, we use quadratic Bézier interpolants that pass through three control interfaces: (1) the free surface $x^1 = \xi^1 = 0$; (2) the bathymetry profile $B(\xi^1 = \zeta, \xi^2)$ where ζ is the seafloor location on the grid; and (3) a flat layer at depth $x^2 = \xi^2 = a$ where a is the bottom of the model (maximum depth). For these constraints, the 2-D vertically deformed coordinate transformation may be expressed as:

$$\begin{bmatrix} x^1 \\ x^2 \end{bmatrix} = \begin{bmatrix} \dfrac{\xi^1(B(\xi^1 - 1) + a\zeta(\zeta - \xi^1))}{\zeta(\zeta - 1)} \\ \xi^2 \end{bmatrix}. \tag{17}$$

Fig. 1 shows the mapping of a mesh in the physical coordinate system (Fig. 1a) to a uniformly sampled grid in the computational domain (Fig. 1b) using the quadratic Bézier curves.

The coordinate mapping in eq. (17) leads to the following covariant metric tensor g_{ij}:

$$g_{ij} = \begin{bmatrix} \dfrac{\left(a\zeta(\zeta - 2\xi^1) + (2\xi^1 - 1)B\right)^2}{\zeta^2(\zeta - 1)} & \dfrac{\xi^1(\xi^1 - 1)\left(a\zeta(\zeta - 2\xi^1) + (2\xi^1 - 1)B\right)B'}{\zeta^2(\zeta - 1)} \\ \dfrac{\xi^1(\xi^1 - 1)\left(a\zeta(\zeta - 2\xi^1) + (2\xi^1 - 1)B\right)B'}{\zeta^2(\zeta - 1)^2} & 1 + \left(\dfrac{\xi^1(\xi^1 - 1)B'}{\zeta(\zeta - 1)}\right)^2 \end{bmatrix}, \tag{18}$$

where B' is the derivative of the bathymetric surface with respect to ξ^2. The associated contravariant metric tensor is:

$$g^{ij} = \begin{bmatrix} [(\xi^1 - 1)\xi^1 B']^2 + (\zeta - 1)^2\zeta^2)\gamma^2 & (\xi^1 - 1)\xi^1 B'\gamma \\ (\xi^1 - 1)\xi^1 B'\gamma & 1 \end{bmatrix}, \tag{19}$$

where $\gamma = [a\zeta(2\xi^1 - \zeta) + B(1 - 2\xi^2)]^{-1}$. Finally, the three independent Christoffel symbols Γ_{11}^1, Γ_{21}^1 and Γ_{22}^1 are given by:

$$\Gamma_{11}^1 = 2(a\zeta - B)\gamma, \tag{20}$$

$$\Gamma_{21}^1 = (1 - 2\xi^1)B'\gamma, \tag{21}$$

$$\Gamma_{22}^1 = \xi^1(1 - \xi^1)B''\gamma. \tag{22}$$

The vector n_j normal to the bathymetric surface can be computed as:

$$n_j = \frac{1}{|\mathbf{n}|}\begin{bmatrix} 1 \\ -B' \end{bmatrix}, \tag{23}$$

where $|\mathbf{n}| = \sqrt{1 + (B')^2}$. These are all geometric objects required in the tensorial acousto- and elastodynamics defined above. Note that these fields depend solely on the 1-D bathymetric surface B and its first- and second-order derivatives B' and B''. Thus, there is a negligible memory overhead associated with the coordinate mapping and geometric variables.
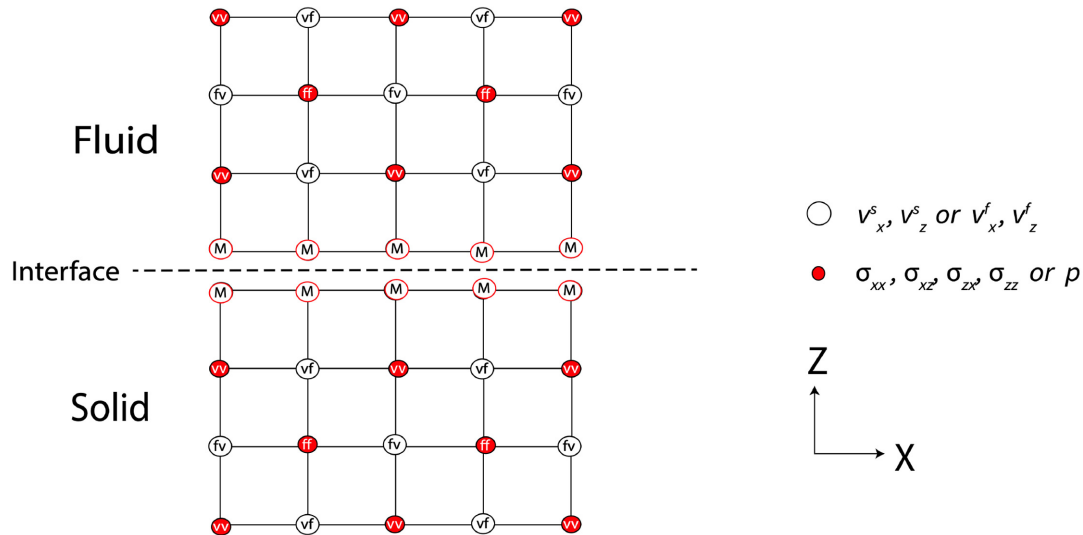
Figure 2. 2-D nodal distribution near a fluid/solid interface. The open circles in the fluid and solid correspond to v_i^f and v_i^s, respectively, defined on the [**f**, **v**] and [**v**, **f**] grids. The red points in the fluid and solid correspond to p and σ_{ij} defined on the [**f**, **f**] and [**v**, **v**] grids. The mimetic points are denoted by M.

4 NUMERICAL IMPLEMENTATION

In this section, we review the split-domain MFD+FSG approach described in Singh *et al.* (2021) for coupled acoustic/elastic media with flat bathymetry and Cartesian grids. Because much of the implementation framework is similar to the Cartesian formulation presented in Singh *et al.* (2021), here we focus on the details required to implement the tensorial approach with bathymetry.

The split-domain MFD+FSG approach involves dividing the model into two computational subdomains corresponding to the fluid and solid media (see Fig. 2) and defining a set of interface grid points on either side of the fluid/solid interface. Fig. 2 also shows the mimetic points (defined at colocated points on both sides of the fluid/solid interface), which are used for updating the field variables. Below we discuss how they are employed to implement the fluid/solid boundary conditions. For each subdomain, we define a 2-D FSG system, equivalent to two coupled SSGs with complementary grid staggerings shifted by half-grid spacing in the horizontal and vertical directions. The discretized pressure p and stress σ_{ij} fields are defined at [**f**, **f**] $\in \mathbb{R}^{(N+2)\times(N+2)}$ and [**v**, **v**] $\in \mathbb{R}^{(N+1)\times(N+1)}$ formed by the [**f**, **f**] and [**v**, **v**] grid nodes, respectively. The discretized particle velocities are defined at [**f**, **v**] $\in \mathbb{R}^{(N+2)\times(N+1)}$ and [**v**, **f**] $\in \mathbb{R}^{(N+1)\times(N+2)}$ formed by the [**f**, **v**] and [**v**, **f**] grid nodes, respectively.

Implementation of the conventional Taylor-series-based FD operators involves many numerical challenges. Their accuracy degrades near the free surface and fluid/solid interfaces, they do not honour flux conservation, and they suffer from long-run stability issues (Castillo & Grone 2003). We address these problems by employing MFD operators. The mimetic divergence and gradient FD operators (**D** and **G**) honour global conservation laws (Castillo & Grone 2003) and can be constructed with high-order accuracy [i.e. $O(\Delta x^4)$ or greater] throughout the entire computational domain including the boundaries and partitioned interfaces (Castillo & Miranda 2013; Corbino & Castillo 2017). These properties make one-sided MFD operators suitable for implementing the boundary conditions with high-order accuracy.

We use numerical mimetic divergence and gradient operators **D** and **G** of $O(\Delta x^4)$ spatial accuracy to compute the wavefield derivatives in eqs (1)–(6) (Singh *et al.* 2021). The mimetic gradient operator **G** acts only on the field variables defined on the **f**-grid and maps them to a vector defined on the **v**-grid. The mimetic divergence matrix operator **D** acts only on the field variables defined on the **v**-grid and maps them to a vector defined on the **f**-grid. In 2-D MFD FSG, the **D** and **G** operators act in both the ξ^1- and ξ^2-directions in a cyclic fashion (Singh *et al.* 2021). For example, to compute the derivative along the ξ^1-direction of σ_{ij} defined on the [**f**, **f**] grid, one needs to apply a mimetic gradient operator **G** that contributes the resulting derivative to v_i defined on the [**v**, **f**] grid. For further details, the reader is referred to Shragge & Tapley (2017) and Singh *et al.* (2021).

The MFD+FSG approach requires applying appropriate weighting for source injection and wavefield extraction due to intertwining of multiple grids (Lisitsa & Vishnevskiy 2010). We perform both injection and extraction in the generalized coordinate system, so first the field variables need to be transformed from the Cartesian to the generalized coordinate system. This transformation for the force vector is defined in eq. (A7). Likewise, for velocity wavefield extraction, the particle-velocity vector can be transformed back to the Cartesian coordinate system using eq. (A10), and then sinc-interpolated to a regularly sampled output mesh for visualization purposes (Shragge 2017). We apply the convolutional perfectly matched layer (C-PML) boundary condition (Martin *et al.* 2008) at all sides of the model except for the free surface.

Table 1. Pseudo-code outlining the steps of the MFD+FSG numerical solution and the relevant equations.

Step	Substep	Instruction	Equation(s)
0		Initialize $v^i(\boldsymbol{\xi})$, $p(\boldsymbol{\xi})$, and $\sigma^{kl}(\boldsymbol{\xi})$	–
1		For all time steps:	–
2		Update $p(\boldsymbol{\xi})$	6
3		Update $v^i_f(\boldsymbol{\xi})$	5
4		Apply PML in fluid subdomain	–
5		Apply free-surface boundary condition	9
6		Update strain tensor	–
	6a	Lower index $v^i(\boldsymbol{\xi}) \rightarrow v_i(\boldsymbol{\xi})$	A6
	6b	Compute $\epsilon_{kl}(\boldsymbol{\xi})$	4
7		Update stress tensor	–
	7a	Transform $\epsilon_{kl}(\boldsymbol{\xi}) \rightarrow \epsilon_{kl}(\boldsymbol{x})$	A13
	7b	Compute $\sigma^{kl}(\boldsymbol{x})$	3
	7c	Transform $\sigma^{kl}(\boldsymbol{x}) \rightarrow \sigma^{kl}(\boldsymbol{\xi})$	A.4 / A12
8		Raise index $v_i(\boldsymbol{\xi}) \rightarrow v^i(\boldsymbol{\xi})$	A.1
9		Inject force source $f^i(\boldsymbol{\xi})$ into $v^i(\boldsymbol{\xi})$	1
10		Apply PML in the solid subdomain	–
11		Apply fluid/solid boundary conditions	–
	11a	Transform $v^i(\boldsymbol{\xi}) \rightarrow v^i(\boldsymbol{x})$ and $\sigma^{kl}(\boldsymbol{\xi}) \rightarrow \sigma^{kl}(\boldsymbol{x})$ on bathymetry	A10 / A13
	11b	Enforce dynamic and kinematic boundary conditions	7 / 8
	11c	Transform $v^i(\boldsymbol{x}) \rightarrow v^i(\boldsymbol{\xi})$ and $\sigma^{kl}(\boldsymbol{x}) \rightarrow \sigma^{kl}(\boldsymbol{\xi})$ on bathymetry	A7 / A12
12		Iterate steps 1–11	–

4.1 Fluid/solid interface FSG implementation

We implement the fluid/solid boundary conditions using a strategy similar to that described in Singh *et al.* (2021), which now accounts for the non-orthogonal components of the vector **n**. The particle-velocity vectors v^s (in the solid subdomain) and v^f (in the fluid subdomain) defined on the [**v**, **f**] and [**v**, **v**] grids at the split-node interface are locally rotated into a Cartesian coordinate system using the rotation operator **R**,

$$\mathbf{R} = \begin{bmatrix} \cos\theta & -\sin\theta \\ \sin\theta & \cos\theta \end{bmatrix}, \tag{24}$$

where one axis is oriented normal to the bathymetric surface at an angle of θ to the vertical. The normal component of the particle-velocity vector is then replaced by $(v_N^s + v_N^f)/2$, where v_N^s and v_N^f are the normal components of the particle-velocity vector in the solid and fluid, respectively, after the rotation:

$$v_N^s = \mathbf{R}v^s \tag{25}$$

$$v_N^f = \mathbf{R}v^f. \tag{26}$$

Similarly, the normal component of stress and pressure is replaced by $(\sigma_{NN}^s - p)/2$, where σ_{NN}^s is the post-rotation value:

$$\sigma_{NN}^s = \mathbf{R}\sigma^s\mathbf{R}^\mathbf{T}. \tag{27}$$

The resulting field variables are then rotated back into the Cartesian coordinate system by replacing **R** with $\mathbf{R}^T$ and vice versa in eqs (25)–(27) above, and transformed to the generalized coordinate system to update the mimetic points shown in Fig. 2. This incurs a moderate computational cost of rotating the field variables along the bathymetric surface, applying the boundary conditions, transforming the field variables back to the Cartesian system, and then again to the generalized coordinate system. For the [**f**, **f**] and [**f**, **v**] sets of nodes, we use the tensorial acoustic and elastic wave equations to update the mimetic points along with the boundary conditions (eqs 7 and 8) using the approach described in Singh *et al.* (2021).

4.2 Pseudo-code for numerical solution

Table 1 presents a pseudo-code for our numerical implementation of the tensorial MFD+FSG algorithm. Steps 2–5 pertain to updating the acoustodynamics solution in the fluid subdomain, steps 6–10 are for updating the elastodynamics solution in the solid subdomain and step 11 implements the fluid/solid boundary conditions. Note that we update the stiffness tensor in step 7 in a Cartesian coordinate system to avoid representing C^{ijkl} in a non-orthogonal coordinate system where the stiffness tensor may become fully populated even for transversely isotropic media with a vertical symmetry axis (VTI) media. A pragmatic approach is to apply Hooke's law in the Cartesian coordinate system and transform the resulting stress tensor back to the generalized coordinate system. This can be done through several floating-point calculations with minimal computational overhead.
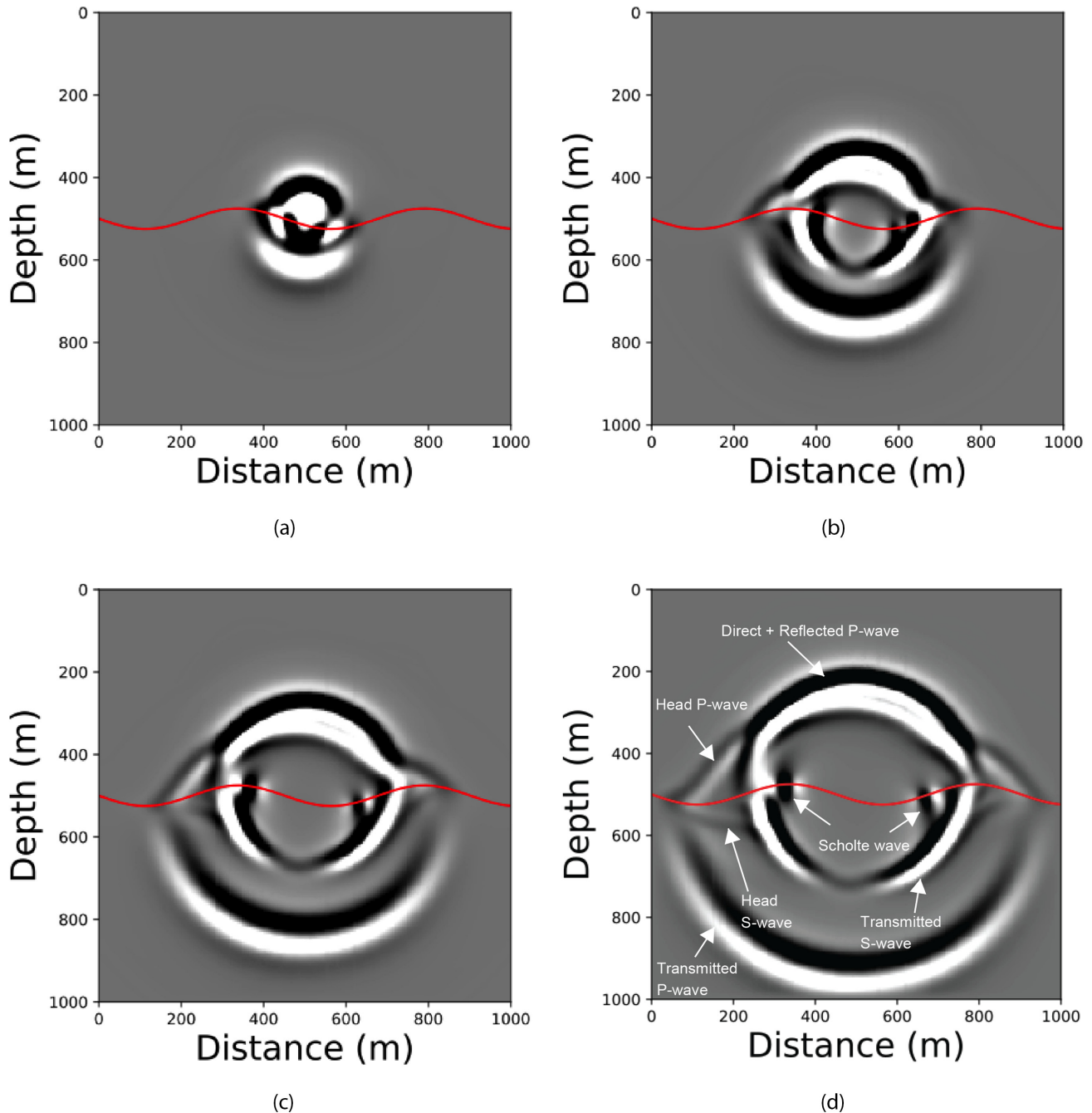
Figure 3. Snapshots of the Cartesian particle-velocity component v_z at (a) $t = 0.375$ s, (b) $t = 0.750$ s, (c) $t = 1.125$ s and (d) $t = 1.250$ s. The bathymetric surface (red) separates the fluid (top) and isotropic solid (bottom) subdomains. The elastic medium is defined by $V_P = 2.5$ km s^{-1}, $V_S = 1.2$ km s^{-1} and density $\rho_S = 2.0$ g cm^{-3}. The velocity and density in the fluid are $c_f = 1.5$ km s^{-1} and $\rho_f = 1.0$ g cm^{-3}, respectively.

5 NUMERICAL EXAMPLES

We test the developed algorithm for models with a fluid/solid interface including both isotropic and anisotropic solids. The resulting solutions are compared with those from the SEM (Komatitsch & Vilotte 1998) to validate the algorithm.

First, we consider a bathymetric surface that represents a sinusoidal function of the lateral x^2-coordinate with the maximum undulations of ± 40 m and a wavelength of 500 m. The medium beneath the surface is elastic and isotropic (Fig. 3). The model size is 100×100 with a grid spacing of $\Delta \xi^1 = \Delta \xi^2 = 10$ m. A 10 Hz Ricker wavelet is injected just above the interface at $[x^1, x^2] = [496, 500]$ m. The simulation progresses for 2500 time steps of $\Delta t = 0.0025$ s. Fig. 3 presents the wavefield snapshots of the velocity component v_z at four different simulation times. The panels show different modes including reflected and transmitted P and S waves, as well as head and surface (Scholte) waves. The numerical simulation is stable and reconstructs all expected arrivals. The close agreement between our solution and that from the
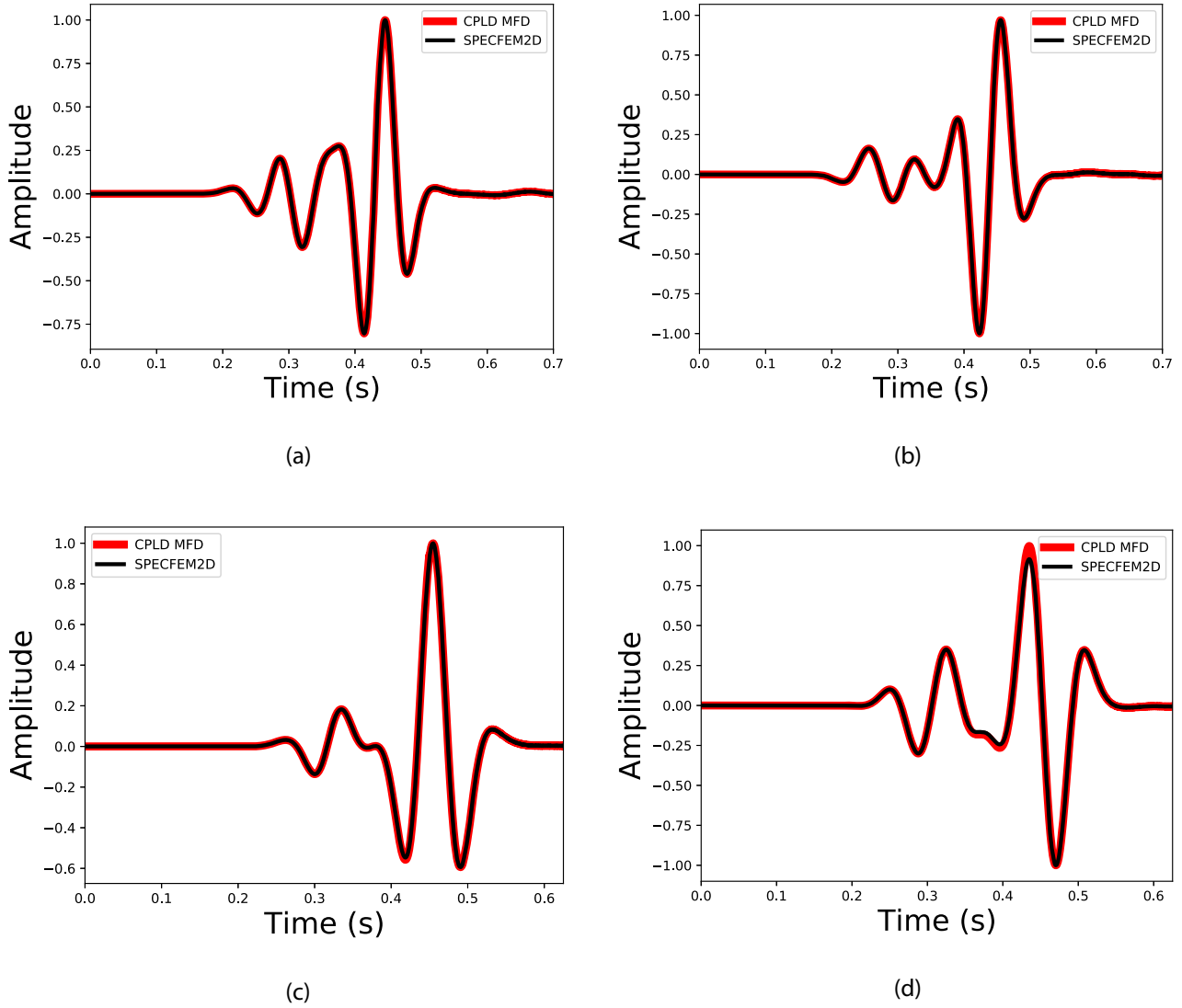
Figure 4. Normalized seismograms for the model in Fig. 3. The red (thick) and black (thin) lines mark the coupled-domain MFD (CPLD MFD) and spectral-element (SPECFEM2D) solutions, respectively. The wavefield components: (a) v_z and (b) v_x at $[x^1, x^2] = [518.6, 190]$ m; (c) v_z and (d) v_x at $[x^1, x^2] = [460, 790]$ m.

SEM (Fig. 4) confirms that the tensorial approach combined with the MFD+FSG implementation (see Table 1) produces accurate results for curved bathymetric surfaces.

For the second example, we consider a tilted bathymetric surface that separates the upper acoustic subdomain from a transversely isotropic medium with a vertical symmetry axis (VTI medium). The model size is 100×100 with a grid spacing of $\Delta \xi^1 = \Delta \xi^2 = 10$ m. A 10 Hz Ricker wavelet is injected in the acoustic medium at $[\xi^1, \xi^2]=[496,500]$ m. Fig. 5 presents snapshots of the v_z-component, which again include body and surface waves, whose propagation is strongly influenced by the bathymetry. Note that the kinematics of the wavefield propagating in the solid is clearly distorted by velocity anisotropy. The agreement between our and SPECFEM2D solutions again confirms the accuracy of the developed method, now for an anisotropic medium (Fig. 6).

For the third and final test, we apply the algorithm to a heterogeneous VTI model generated by Hess with the Thomsen parameters shown in Fig. 7. The solid VTI subdomain is separated from the acoustic subdomain by the shallow bathymetry profile. The model size is 250×250 with the grid spacing $\Delta \xi^1 = \Delta \xi^2 = 4$ m. We inject a 25 Hz source wavelet at $[x^1, x^2] = [50, 500]$ m. The results presented in Fig. 8 demonstrate that the coupled acoustic/elastic anisotropic MFD+FSG algorithm can model numerically stable, complex wavefields for vertically and laterally heterogeneous anisotropic media beneath an undulating bathymetric surface.

6 DISCUSSION

The tensorial MFD+FSG algorithm that uses a family of 2-D vertically deformed coordinate systems provides an efficient way to compute elastic wavefield solutions for coupled fluid/solid media. The developed theory is discussed in detail only for 2-D fluid/solid models but the
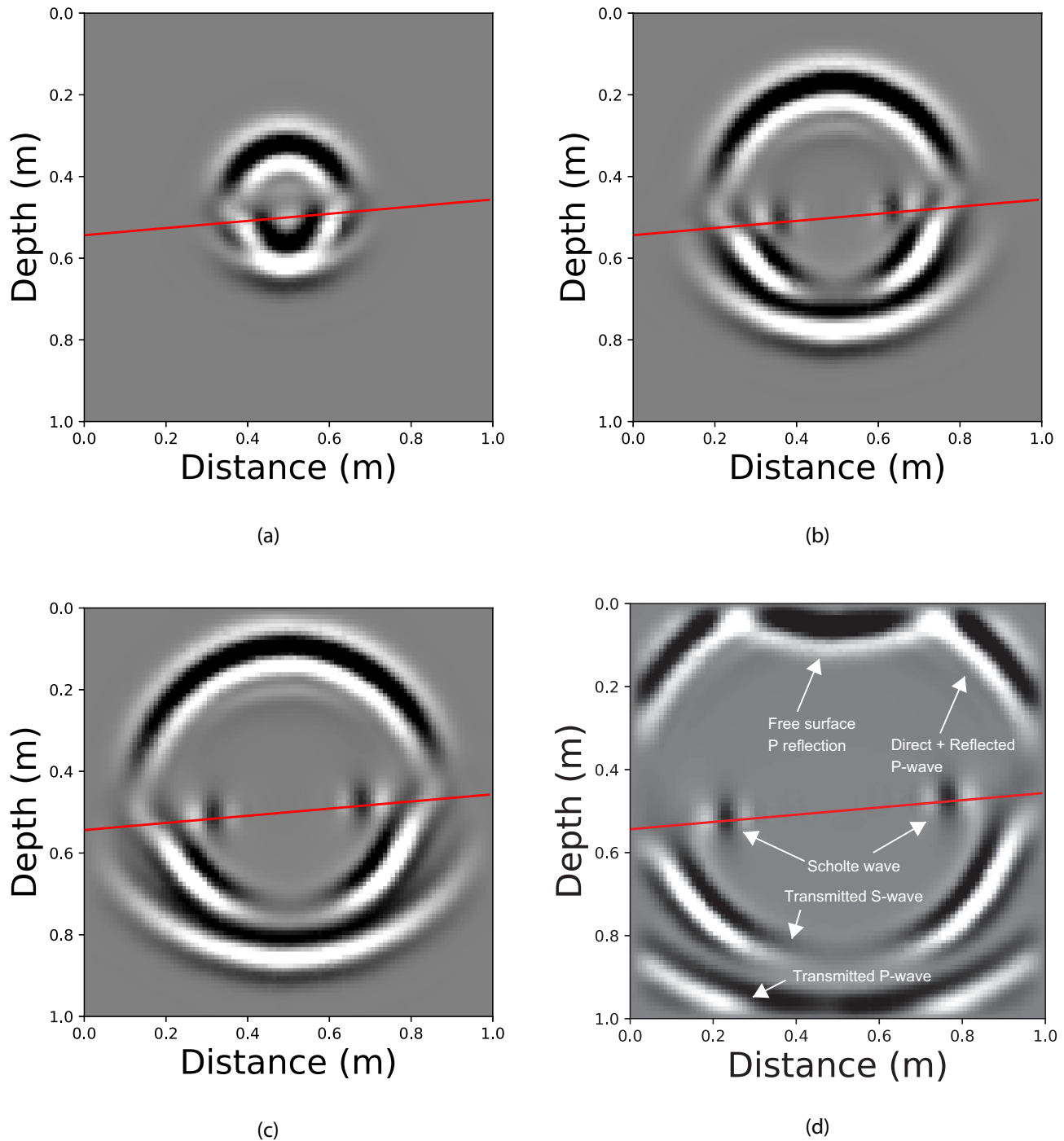
Figure 5. Snapshots of the component v_z at (a) $t = 0.15$ s, (b) $t = 0.25$ s, (c) $t = 0.30$ s and (d) $t = 0.40$ s. The bathymetric surface (red) separates a fluid (top) and a VTI solid (bottom). The VTI medium is defined by the following Thomsen parameters (see Tsvankin 2012): the *P*-wave vertical velocity $V_{P0} = 1.7$ km s^{-1}, the *S*-wave vertical velocity $V_{S0} = 1.2$ km s^{-1}, and the anisotropy coefficients $\epsilon = 0.2$ and $\delta = 0.1$; the density $\rho_S = 1.5$ g cm^{-3}. The velocity and density in the fluid are $c_f = 1.5$ km s^{-1} and $\rho_f = 1.0$ g cm^{-3}.

extension to 3-D is straightforward. The acousto- and elastodynamics theory outlined in the Theory section is valid for any 3-D generalized coordinate system. However, the vertically deformed coordinate system needs to be extended along the x^3-axis using a linear transformation $(x^3 = \xi^3)$. This increases the number of non-zero independent Christoffel symbols from three to six (2-D to 3-D), but the general expressions (e.g. eq. 13) and the sparseness of the other geometric field variables remain the same.
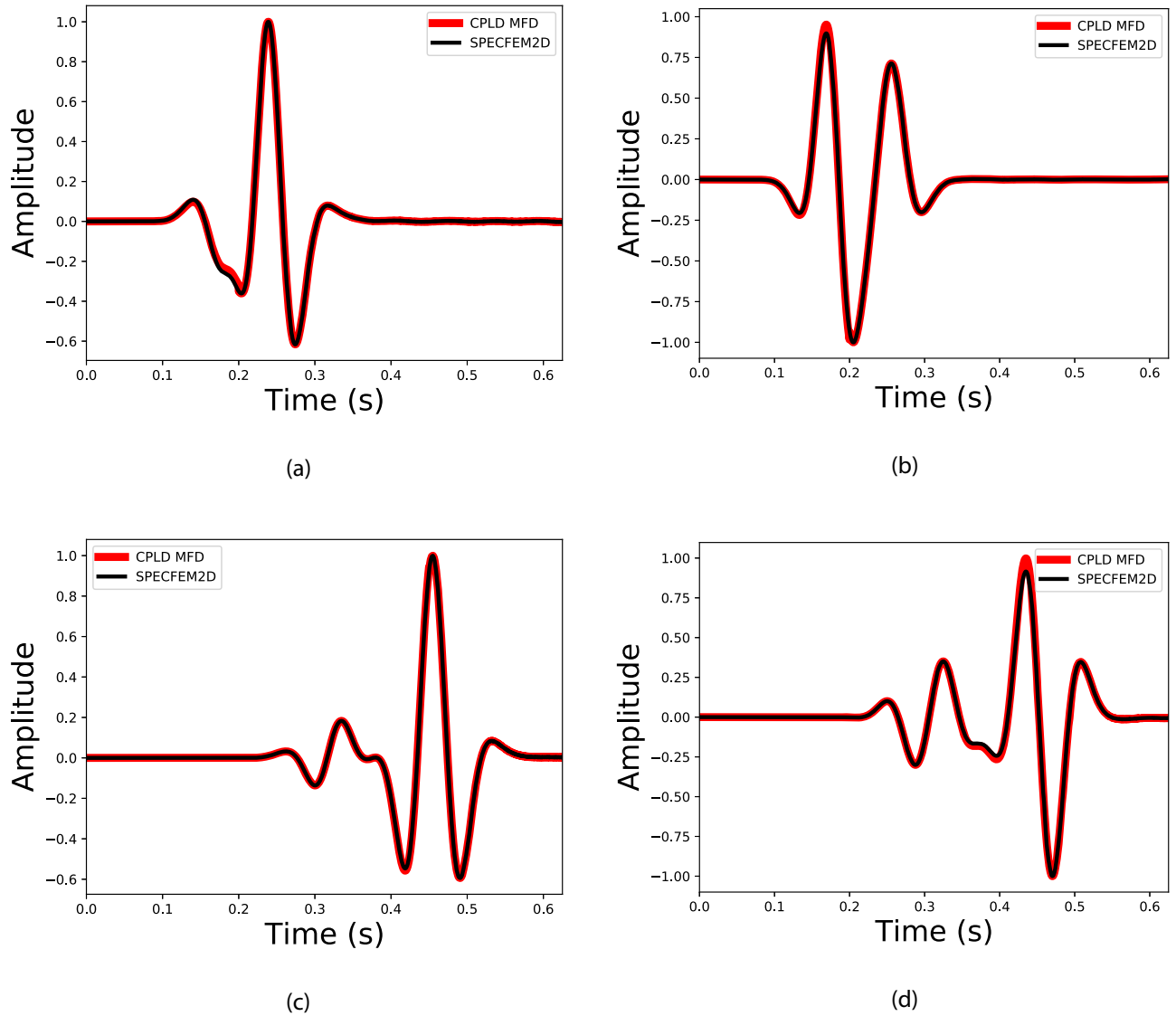
Figure 6. Normalized seismograms for the model in Fig. 5. The red (thick) and black (thin) lines mark the coupled-domain MFD (CPLD MFD) and spectral-element (SPECFEM2D) solutions, respectively. The wavefield components: (a) v_z and (b) v_x at $[x, z] = [400, 505.2]$ m; (c) v_z and (d) v_x at $[x, z] = [800, 470.3]$ m.

The non-orthogonal coordinate transformations using analytic mapping discussed herein allow users to avoid expensive 3-D meshing operations. However, the staggered-grid formulation combined with the chain-rule approach in eq. (16) involves additional partial wavefield derivative computations. For 2-D applications the number of the required partial derivatives in the anisotropic elastic medium increases from 8 to 15, as compared to the Cartesian wave equation, using quadratic Bézier curves for the coordinate transformation.

The vertically deformed meshes do not impose any orthogonality restrictions on the computational meshes. However, the wavefield solutions on these meshes are still subject to the Courant–Frederich–Lewy (CFL) criterion for choosing the time step size for the discretized system. Note that the grid-element size in Fig. 1(a) varies spatially. Therefore, the grid-element size in Fig. 1(b) has to be chosen carefully so that the smallest element in the grid does not become too small or too large in the physical space in Fig. 1(a). The CFL conditions depend on the smallest grid-element size in the physical space, while numerical dispersion is difficult to control if that size becomes too large.

Finally, we note that the depth of flat bathymetry in the generalized coordinate system (i.e. ζ) is controlled by the maximum water depth in the physical space. In the above examples, we have chosen ζ to be the ratio of the maximum water depth to the total thickness (i.e. a) of the model. Because the numerical mapping approach assumes a constant number of grid points in the acoustic and elastic domains at each horizontal coordinate location, it can be challenging to simulate seismic waves if the bathymetry changes significantly over the modelled area. An extreme example of this would be for models involving transitions from land through a shelf break to deep water. Handling such cases, while possible with a coupled-domain approach using tensorial FD methods, would require more complicated meshing procedure and
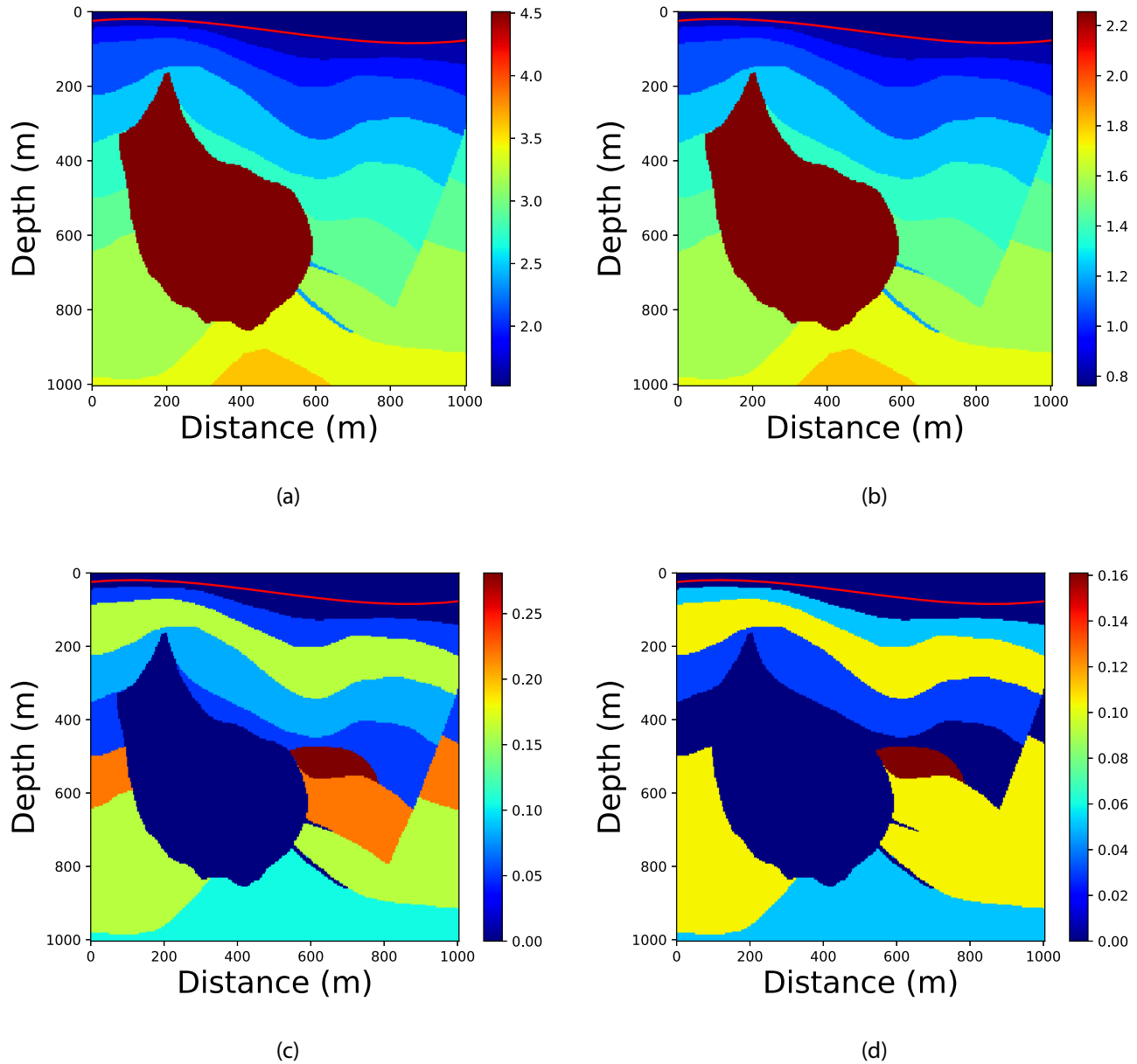
Figure 7. Hess VTI model defined by the Thomsen (1986) parameters (see also Tsvankin 2012): (a) V_{P0} (in km s^{-1}), (b) V_{S0} (in km s^{-1}), (c) ϵ, and (d) δ. The red line denotes the bathymetric surface beneath the water layer. The parameters V_{S0}, ϵ and δ are not defined in the acoustic subdomain, where their values are shown as zeros.

numerical implementation than the one presented here. Thus, the modelling approach presented herein is not a panacea for all possible marine bathymetry scenarios.

7 CONCLUSIONS

We developed a novel approach to full-wavefield modelling for coupled acoustic/elastic anisotropic media that include complex bathymetric interfaces. Employing the contravariant representation of the stress and stiffness tensors makes it possible to retain the well-known tensor symmetries in an arbitrary coordinate system. Semi-analytic coordinate mapping helps implement a computationally and memory-efficient numerical approach that enforces the correct boundary conditions and produces the entire wavefield including body and surface waves. The modelling results and comparison with the spectral-element method confirm that our MFD+FSG algorithm accurately simulates wavefields even for strongly undulating bathymetric surfaces overlying structurally complex anisotropic media.
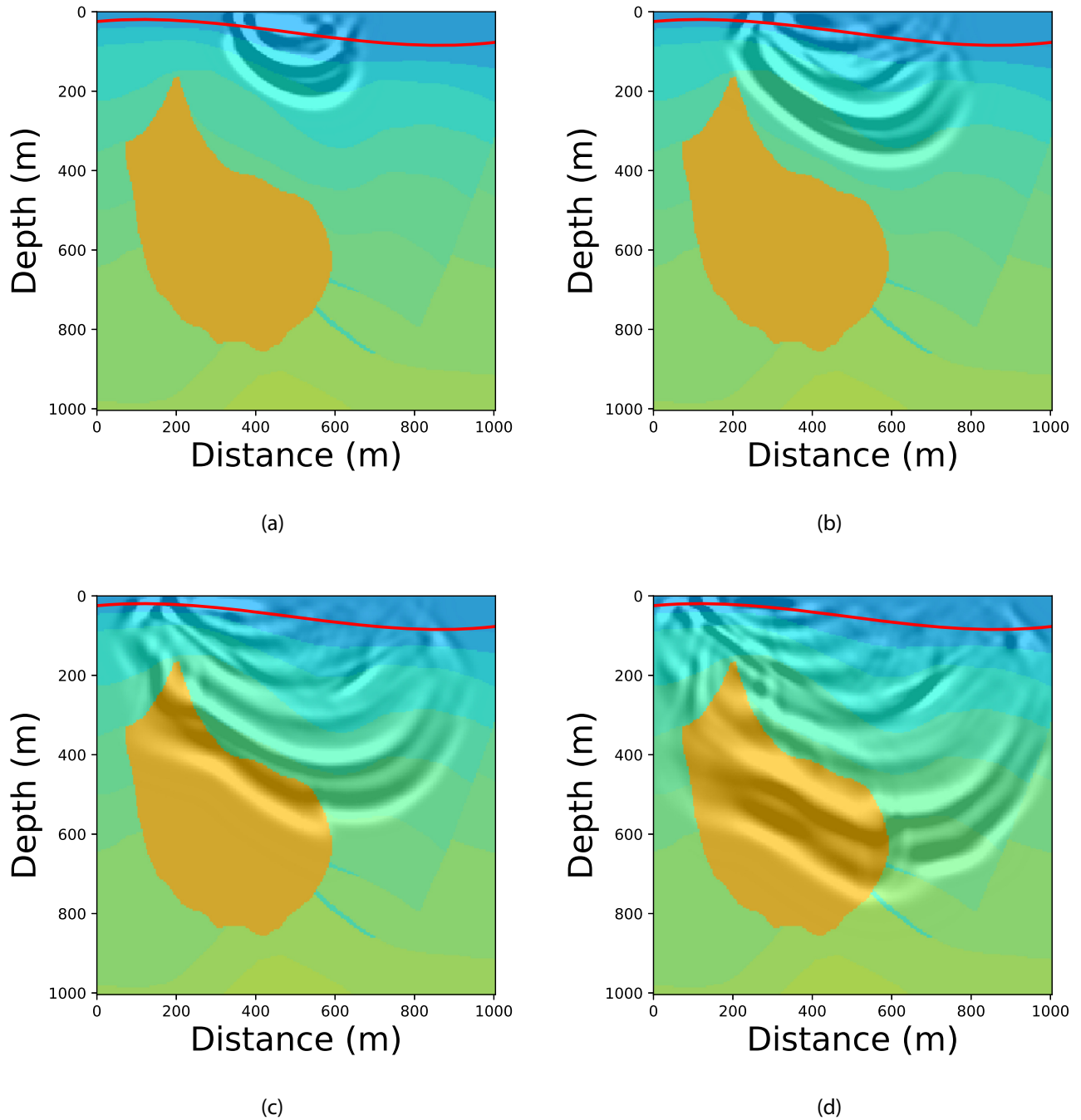
Figure 8. Snapshots of the v_z-component for the model from Fig. 7 at times (a) $t = 0.15$ s, (b) $t = 0.20$ s, (c) $t = 0.30$ s, and (d) $t = 0.40$ s.

DATA AVAILABILITY

Data associated with this research are available and can be obtained by contacting the corresponding author.

REFERENCES

Appelö, D. & Petersson, N. A., 2009. A stable finite difference method for the elastic wave equation on complex geometries with free surfaces, *Commun. Comput. Phys.,* **5**(1), 84–107.

Brillouin, L. & Brennan, R. O., 1965. *Tensors in Mechanics and Elasticity,* American Society of Mechanical Engineers Digital Collection.

Castillo, J. E. & Grone, R., 2003. A matrix analysis approach to higher-order approximations for divergence and gradients satisfying a global conservation law, *SIAM J. Matrix Anal. Appl.,* **25**(1), 128–142.

Castillo, J. E. & Miranda, G. F., 2013. *Mimetic Discretization Methods,* Chapman and Hall/CRC.

Chaljub, E., Capdeville, Y. & Vilotte, J.-P., 2003. Solving elastodynamics in a fluid–solid heterogeneous sphere: a parallel spectral element approximation on non-conforming grids, *J. Comput. Phys.,* **187**(2), 457–491.

Corbino, J. & Castillo, J., 2017. *Computational Science and Engineering,* San Diego State University.

de Hoop, A. T. & Van der Hijden, J. H., 1984. Generation of acoustic waves by an impulsive point source in a fluid/solid configuration with a plane boundary, *J. acoust. Soc. Am.,* **75**(6), 1709–1715.

de la Puente, J., Ferrer, M., Hanzich, M., Castillo, J. E. & Cela, J. M., 2014. Mimetic seismic wave modeling including topography on deformed staggered grids, *Geophysics,* **79**(3), T125–T141.

Flügge, W., 1972. *Tensor Analysis and Continuum Mechanics,* Springer.

Fornberg, B., 1988. The pseudospectral method: accurate representation of interfaces in elastic wave calculations, *Geophysics,* **53**(5), 625–637.

Ge, Z. & Chen, X., 2007. Wave propagation in irregularly layered elastic models: a boundary element approach with a global reflection/transmission matrix propagator, *Bull. seism. Soc. Am.,* **97**(3), 1025–1031.

Hestholm, S. & Ruud, B., 1994. 2d finite-difference elastic wave modelling including surface topography 1, *Geophys. Prospect.,* **42**(5), 371–390.

Käser, M. & Dumbser, M., 2008. A highly accurate discontinuous Galerkin method for complex interfaces between solids and moving fluids, *Geophysics,* **73**(3), T23–T35.

Komatitsch, D. & Vilotte, J., 1998. The spectral-element method: an efficient tool to simulate the seismic response of 2D and 3D geological structures, *Bull. seism. Soc. Am.,* **2**, 368–398.

Komatitsch, D., Coutel, F. & Mora, P., 1996. Tensorial formulation of the wave equation for modelling curved interfaces, *J. geophys. Int.,* **127**(1), 156–168.

Komatitsch, D., Barnes, C. & Tromp, J., 2000. Wave propagation near a fluid-solid interface: a spectral-element approach, *Geophysics,* **65**(2), 623–631.

Konuk, T. & Shragge, J., 2021. Tensorial elastodynamics for anisotropic media, *Geophysics,* **86**(4), T1–T60.

Lisitsa, V. & Vishnevskiy, D., 2010. Lebedev scheme for the numerical simulation of wave propagation in 3d anisotropic elasticity, *Geophys. Prospect.,* **58**(4), 619–635.

Martin, R., Komatitsch, D. & Gedney, S. D., 2008. A variational formulation of a stabilized unsplit convolutional perfectly matched layer for the isotropic or anisotropic seismic wave equation, *Comput. Model. Eng. Sci.,* **37**(3), 274–304.

McConnell, A. J., 2014. *Applications of Tensor Analysis,* Courier Corporation.

Padilla, F., de Billy, M. & Quentin, G., 1999. Theoretical and experimental studies of surface waves on solid–fluid interfaces when the value of the fluid sound velocity is located between the shear and the longitudinal ones in the solid, *J. acoust. Soc. Am.,* **106**(2), 666–673.

Shragge, J., 2017. Tensorial elastodynamics for isotropic media on vertically deformed meshes, in *SEG Technical Program Expanded Abstracts 2017,* pp. 4034–4038, Society of Exploration Geophysicists.

Shragge, J. & Konuk, T., 2020. Tensorial elastodynamics for isotropic media, *Geophysics,* **85**(6), T359–T373.

Shragge, J. & Tapley, B., 2017. Solving the tensorial 3D acoustic wave equation: a mimetic finite-difference time-domain approach, *Geophysics,* **82**(4), T183–T196.

Singh, H., Shragge, J. & Tsvankin, I., 2021. Mimetic finite-difference coupled-domain solver for anisotropic media, *Geophysics,* **86**(1), T45–T59.

Sun, Y.-C., Zhang, W., Xu, J.-K. & Chen, X., 2017. Numerical simulation of 2-D seismic wave propagation in the presence of a topographic fluid–solid interface at the sea bottom by the curvilinear grid finite-difference method, *J. geophys. Int.,* **210**(3), 1721–1738.

Tarrass, I., Giraud, L. & Thore, P., 2011. New curvilinear scheme for elastic wave propagation in presence of curved topography, *Geophys. Prospect.,* **59**, 889–906.

Tessmer, E., Kosloff, D. & Behle, A., 1992. Elastic wave propagation simulation in the presence of surface topography, *J. geophys. Int.,* **108**(2), 621–632.

Thomsen, L., 1986. Weak elastic anisotropy, *Geophysics,* **51**, 1954–1966.

Tsvankin, I., 2012. *Seismic Signatures and Analysis of Reflection Data in Anisotropic Media,* Society of Exploration Geophysicists, 3rd edn.

Van Vossen, R., Robertsson, J. O. & Chapman, C. H., 2002. Finite-difference modeling of wave propagation in a fluid–solid configuration, *Geophysics,* **67**(2), 618–624.

Virieux, J., 1986. P-sv wave propagation in heterogeneous media: velocity-stress finite-difference method, *Geophysics,* **51**(4), 889–901.

Voinovich, P., Merlen, A., Timofeev, E. & Takayama, K., 2003. A Godunov-type finite-volume scheme for unified solid-liquid elastodynamics on arbitrary two-dimensional grids, *Shock Waves,* **13**(3), 221–230.

Wilcox, L. C., Stadler, G., Burstedde, C. & Ghattas, O., 2010. A high-order discontinuous Galerkin method for wave propagation through coupled elastic–acoustic media, *J. Comput. Phys.,* **229**(24), 9373–9396.

Zhang, J., 2004. Wave propagation across fluid—solid interfaces: a grid method approach, *J. geophys. Int.,* **159**(1), 240–252.

Zhang, W. & Chen, X., 2006. Traction image method for irregular free surface boundaries in finite difference seismic wave simulation, *J. geophys. Int.,* **167**(1), 337–353.

APPENDIX A—COORDINATE TRANSFORMATION, METRIC TENSOR AND CHRISTOFFEL SYMBOLS

In a Cartesian coordinate system, there is no distinction between covariant, contravariant and mixed tensor components; however, this is not the case for generalized coordinate representations. This appendix provides a mathematical primer for the generalized framework discussed above, including descriptions of the metric tensor, Christoffel symbols, basis transformations, coordinate transformations and calculus operations performed in the generalized coordinates.

A.1 Metric tensor and Christoffel symbols

The metric tensor is a fundamental geometric object that provides a tensor measure of how the local space expands, contracts or shears under coordinate mappings defined by $x = x(\xi)$ and $\xi = \xi(x)$, where x and ξ are the Cartesian and generalized coordinate variables, respectively.

The components of the metric tensor g_{ij} in the covariant representation are given by:

$$g_{ij} = \frac{\partial x^k}{\partial \xi^i} \frac{\partial x^k}{\partial \xi^j}. \tag{A1}$$

The contravariant (or inverse) metric tensor can be computed as:

$$g^{ik} g_{ij} = \delta_j^k. \tag{A2}$$

In matrix notation, this operation can be represented through an inverse operation:

$$\left[g^{ij} \right] = \left[g_{ij} \right]^{-1}. \tag{A3}$$

The Christoffel symbols Γ_{ij}^k are computed from the metric tensor according to

$$\Gamma_{ij}^k = \frac{1}{2} g^{kl} \left(\frac{\partial g_{li}}{\partial \xi_j} + \frac{\partial g_{lj}}{\partial \xi_i} - \frac{\partial g_{ij}}{\partial \xi_l} \right). \tag{A4}$$

The partial derivatives in eq. (A4) are measures of the spatial variation of the metric tensor g_{ij}. Christoffel symbols do not formally represent tensors because they do not obey tensor transformation rules, but have the symmetries $\Gamma_{ij}^k = \Gamma_{ji}^k$ that we exploit above.

A.2 Basis transformations

The above framework requires transformation between contravariant and covariant tensor forms, which can be accomplished through index raising and lowering operations. For a rank-one tensor, a contravariant tensor can be obtained from its covariant form via raising the index through contraction with the contravariant metric tensor:

$$f^i = g^{ij} f_j. \tag{A5}$$

Similarly, we may write the index-lowering operation as:

$$f_i = g_{ij} f^j. \tag{A6}$$

For rank-two tensors, one generally applies raising and lowering transformations to both indices.

A.3 Coordinate transformations

Switching between the Cartesian and generalized coordinate systems requires implementing a tensor coordinate transformation. Here, we present forward and inverse coordinate transforms between the Cartesian and generalized coordinates for rank-one and rank-two tensors defined in the contravariant basis. The forward transformation of a rank-one tensor from the Cartesian to the generalized coordinates is given by:

$$v^i \big|_\xi = Q_j^i v^j \big|_x, \tag{A7}$$

where Q_j^i is the following partial derivative that involves both coordinate systems:

$$Q_j^i = \frac{\partial x^i}{\partial \xi^j}. \tag{A8}$$

Eq. (A8) can be rewritten in matrix form:

$$Q_j^i = \begin{bmatrix} Q_1^1 & Q_2^1 & Q_3^1 \\ Q_1^2 & Q_2^2 & Q_3^2 \\ Q_1^3 & Q_2^3 & Q_3^3 \end{bmatrix}. \tag{A9}$$

For a rank-one tensor, the inverse coordinate mapping from the generalized to the Cartesian coordinates is defined by:

$$v^j \big|_x = A_i^j v^i \big|_\xi, \tag{A10}$$

where the inverse coordinate transformation A_i^j is:

$$A_l^k Q_j^i = \delta_i^k \delta_j^l. \tag{A11}$$

Similarly, both components of the rank-two tensor σ^{ij} undergo a coordinate transformation according to:

$$\sigma^{kl} \big|_\xi = Q_i^k Q_j^l \sigma^{ij} \big|_x. \tag{A12}$$

The inverse coordinate transformation is described by:

$$\sigma^{ij} \big|_x = A_k^i A_l^j \sigma^{kl} \big|_\xi. \tag{A13}$$

Similar coordinate transformations can be developed for rank-one and rank-two covariant tensors.

A.4 Calculus operations

In a generalized coordinate system, the contravariant basis vectors $\hat{g}^i$ are unlikely to be orthonormal. Thus, one must define standard calculus operations to account for their geometric variations. The gradient of a scalar field is:

$$\nabla_i \phi = g^{ij} \frac{\partial \phi}{\partial \xi^i} \equiv c^j, \tag{A14}$$

where c^j denotes the contravariant gradient component in the *j*th direction. The divergence of a vector field with the contravariant components V^i is:

$$\nabla_i V^i = \frac{\partial V^i}{\partial \xi^i} + \Gamma^l_{il} V^i = \frac{1}{\sqrt{|g|}} \frac{\partial}{\partial \xi^i} \left(\sqrt{|g|} V^i \right), \tag{A15}$$

where the final equality is known as the Voyl–Weyl formula. Similarly, the divergence of the second-order contravariant tensor T^{ij} has the form:

$$\nabla_i T^{ij} = \frac{\partial T^{ij}}{\partial \xi_i} + \Gamma^i_{ik} T^{kj} + \Gamma^j_{ik} T^{ik}. \tag{A16}$$

APPENDIX B—MAPPING EQUATIONS

Here, we derive the vertical mapping function that uses quadratic Bézier interpolants to connect three control surfaces: (1) the free surface; (2) the bathymetric profile and (3) the base of the mesh. Surfaces (1) and (3) are assumed to be flat.

Suppose P_0, P_1 and P_2 are the control points, and P_c is the fixed point that the curve passes through. Then, the quadratic Bézier curve is defined by:

$$x^1 = P(\xi^1) = P_0(1 - \xi^1)^2 + P_1 2(1 - \xi^1)\xi^1 + P_2(\xi^1)^2, \tag{B1}$$

where $\xi^1 \in [0, 1]$. There are an infinite number of solutions that might pass through that point for any value of ξ^1. Picking one of them (e.g. $\xi^1 = \zeta$), equating this to control point P_c,

$$P_c \big|_{\xi^1 = \zeta} = P_0(1 - \zeta)^2 + P_1 2\zeta(1 - \zeta) + P_2\zeta^2, \tag{B2}$$

and solving for P_1 yields:

$$P_1 = \frac{P_c - P_0(1 - \zeta^2) - P_2\zeta^2}{2\zeta(1 - \zeta)}. \tag{B3}$$

For the problem at hand the control point $P_c = B$ represents the bathymetric surface at the coordinate $\xi^2 = x^2$, $P_0 = 0$ is the water surface, and $P_2 = a$ is the depth where $a > \max(B)$. Introducing these points into eq. (B3) results in:

$$P_1 = \frac{B - a\zeta^2}{2\zeta(1 - \zeta)}. \tag{B4}$$

This means that the 1-D mapping function is given by:

$$x^1 = P(\xi^1) = \frac{2(1 - \xi^1)\xi^1(B - a\zeta^2) + 2\zeta(1 - \zeta)a(\xi^1)^2}{2\zeta(1 - \zeta)}. \tag{B5}$$

Simplifying eq. (B5) leads to the following expression:

$$x^1 = P(\xi^1) = \frac{\xi^1 \left(B(\xi^1 - 1) + a\zeta(\zeta - \xi^1) \right)}{\zeta(\zeta - 1)}. \tag{B6}$$

Note that (1) for the free surface $\xi^1 = 0$, so $x^1 = P(\xi^1) = 0$; (2) at the base of the mesh $\xi^1 = 1$, so $x^1 = P(\xi^1) = a$ and (3) when $\xi^1 = \zeta$, eq. (B5) reduces to $P(\zeta) = B$.

Because $\xi^1 \in [0, 1]$, the ξ^1 coordinate can be defined numerically on a **v**-grid with $N + 1$ points (i.e. from 0 to N) according to:

$$\xi^1 = \frac{n}{N}, \quad 0 \le n \le N + 1, \tag{B7}$$

and an **f**-grid with $N + 2$ points by:

$$\xi^1 = \begin{cases} 0 & n = 0, \\ \dfrac{n - 1/2}{N} & 1 < n \le N + 1, \\ 1 & n = N + 2. \end{cases} \tag{B8}$$